

20 **Abstract**

21

22 The 2019-2020 Southwest Puerto Rico earthquake sequence ruptured multiple faults with
23 several moderate magnitude earthquakes. Here we investigate the seismotectonics of this fault
24 system using high precision hypocenter relocation and inversion of the near-field strong
25 motions of five largest events in the sequence ($5.6 \leq M_w \leq 6.4$) for kinematic rupture models.
26 The $M_w 6.4$ mainshock occurred on an NE striking, SE dipping normal fault. The rupture
27 nucleated offshore ~ 15 km SE of Indios at the depth of 8.6 km and extended SW-NE and up-
28 dip with an average speed of 1.55 km/s, reaching the seafloor and shoreline after about 8
29 seconds. The 6th of January, 2020 (10:32:23) $M_w 5.7$ and the 7th of January, 2020 (11:18:46)
30 $M_w 5.8$ events occurred on two E-SE striking, near-vertical, left-lateral strike-slip faults.
31 However, the 7th January, 2020 (08:34:05) $M_w 5.6$ normal faulting aftershock which occurred
32 only 10 minutes after the $M_w 6.4$ normal faulting mainshock, ruptured on a fault with almost
33 the same strike as the mainshock but situated ~ 8 km further E, forming a set of parallel faults
34 in the fault system. On 11th January 2020, a $M_w 6.0$ earthquake occurred on a N-NE striking,
35 W dipping fault, orthogonal to the faults hosting the strike-slip earthquakes. We apply template
36 matching for the detection of missed, small magnitude earthquakes to study the spatial
37 evolution of the main part of the sequence. Using the template matching results along with
38 GPS analysis, we image the temporal evolution of a foreshock sequence (Caja swarm). We
39 propose that the swarm and the main sequence were a response to a tectonic transient that most
40 affected the whole Puerto Rico island.

41 1. Introduction

42

43 The 2019-2020 Southwest Puerto Rico earthquake sequence included multiple moderate
44 earthquakes ($M_w > 5.0$) that ruptured different faults with different faulting mechanisms
45 (University of Puerto Rico, 1986). The swarm-like earthquake sequence started in July 2019
46 with a smaller offshore Caja swarm, 14 km south of Ponce, Puerto Rico. The activity continued
47 with the main sequence starting on December 28th, 2019 comprising more than 10 $M_w \geq 5.0$
48 earthquakes and the largest, $M_w 6.4$, normal faulting earthquake on January 7th 2020.

49 The island of Puerto Rico (Fig. 1) is located in a zone of convergence between the North
50 American (NAP) and Caribbean (CP) tectonic plates (Huérffano et al., 1994). North of the
51 island, the NAP is subducting obliquely beneath the CP at the rate of (20 ± 0.4) mm/yr (DeMets
52 et al., 2010) along the east-west striking Puerto Rico trench. Oblique subduction results in
53 strain partitioning and favours microplate tectonics along the eastern Great Antilles island arc
54 (Jansma et al., 2005). The Puerto Rico microplate (PRm) is part of the CP and is moving ENE
55 relative to NAP (Jansma et al., 2000). On the southern margin of the PRm, the CP is subducting
56 under the Greater Antilles crust (van Benthem et al., 2013). Slip rates derived from GPS
57 velocities estimate convergence between 3mm/yr south of Hispaniola island and 0.2mm/yr
58 south of Puerto Rico (Benford et al., 2012, Granja-Bruna et al., 2010).

59

60 Rare moderate size earthquakes occurred in and near Puerto Rico in the 20th century and earlier
61 (Reid et al., 1919, Doser et al., 2005). The majority of instrumental earthquakes ($M_w \geq 3.0$) is
62 located north of the island, along the NAP subduction zone. Seismically most active are the
63 SW and SE regions of Puerto Rico (Huérffano et al., 2005). The shallow seismicity of southern
64 Puerto Rico is related to the internal deformation within the Puerto Rico fault zone in the NW-

65 SE direction, while the intermediate depth seismicity occurs above a north dipping zone
66 beneath the island (Huérfano et al., 2005). The tectonics of the southern part of the island is
67 partially controlled by E-W oriented strike-slip faults; South Lajas, Punta Montalva and Salinas
68 faults, which form a more than 80km long fault system. Recent paleoseismologic studies
69 showed that some of the strike-slip faults in the SW of Puerto Rico ruptured in the last 10,000
70 years and pose a considerable seismic hazard. The South Lajas fault experienced two surface
71 rupturing events, around 5,000 years ago (Prentice and Mann, 2005), while the Salinas fault
72 ruptured twice in the past 10,400 years (Piety et al., 2018).

73 We study the geometry (Fig. 1) of the faults activated in the SW of Puerto Rico during the
74 2019-2020 Southwest Puerto Rico sequence by relocating the sequence and performing the
75 kinematic source-rupture modelling of the five largest events ($5.6 < M_w < 6.4$). The relocated
76 events and kinematic rupture inversion reveal a sequence that activated a parallel set of WNW-
77 ESE striking strike-slip faults, connected by an orthogonal, NNE-SSW strike-slip fault and
78 oblique, NE-SW striking normal faults. We adopt the matched filter event detection approach
79 to study the temporal and spatial evolution along the faults and in combination with GPS data
80 analysis. We suggest that the sequence was preceded by a transient deformation that most likely
81 loaded the system.

82 **2. Methods**

83

84 We obtained an earthquake catalog for the Puerto Rico area (N17.56° N18.73°, E-65.50° to E-
85 67.80°) from 2019-01-01 to 2020-05-02, $M \geq 2.0$ through United States Geological Survey
86 (USGS) (Benz, 2017) including corresponding PRSN and USGS P and S arrival times, time
87 uncertainties and first-motions. This catalog contains 7,054 events. We obtained from IRIS-
88 DMC metadata for permanent and temporary stations used for relocation (within 1° around the
89 epicenter of $M_w 6.5$ mainshock, see Fig. S3) and waveforms for coherence analysis, matched-
90 filter and kinematic source analysis.

91

92 2.1. Precise, absolute earthquake locations

93 We obtained absolute relocations for the study area using source-specific, station travel-time
94 corrections (SSST; Richards-Dinger & Shearer, 2000) and high-precision relocation based on
95 waveform coherency between events. This approach produces enhanced relative location and
96 clustering of events, and allows analysis of model- and data-dependent error in the hypocenters
97 (Lomax, 2020). We performed absolute earthquake location with the NonLinLoc algorithm
98 (Lomax et al., 2000, 2014; NLL hereafter), which uses efficient global sampling algorithms to
99 obtain an estimate of the posterior probability density function (PDF) in 3D space for absolute
100 hypocenter location. The location PDF provides a complete description of likely hypocentral
101 locations, includes comprehensive uncertainty information, and allows robust application of
102 waveform coherency relocation. Within NLL, we used the equal differential-time (EDT)
103 likelihood function (Font et al., 2004; A. Lomax, 2005, 2008; Lomax et al., 2014; Zhou, 1994),
104 which is very robust in the presence of outlier data caused by large error in the arrival-times or
105 predicted travel-times. We performed all locations using a search range in depth from 1 to 60

106 km depth. The shallow limit is a prior constraint required to suppress unreasonably shallow,
107 maximum likelihood depths for numerous events which exhibit double PDF solutions in depth.
108 We used a smoothed, minimum 1D P wave velocity model (Fig. S1) for Puerto Rico and the
109 U.S. Virgin Islands (Huérfano et al., 2010) to seed NLL SSST relocation. We used a finite-
110 differences, eikonal-equation algorithm (Podvin & Lecomte, 1991) to calculate travel-times
111 for P phases for each station, and obtained S phase travel times from these P times through
112 $V_p/V_s=1.71$.

113 We relocated events in the Puerto Rico catalog in two stages. First, starting with the initial NLL
114 locations without station corrections, we iteratively generated SSST corrections which vary
115 smoothly within a 3D volume to provide a source-position dependent correction for each
116 station and phase type. We used smoothing distances of 32, 16, 8 and 4 km. Only P and S
117 arrivals with residuals of ≤ 2.0 sec for relocated events meeting minimum quality criteria (68%
118 error-ellipsoid principle-axis half-width ≤ 10 km, root mean square of residuals (rms) ≤ 0.2
119 sec, number of phase readings ≥ 12 , azimuth gap $\leq 220^\circ$) are used for update at each iteration.
120 See supplementary material Methods S1 for more details. We relocated the full catalog using
121 the 5 km smoothing-length, SSST corrections (Fig. S2a). In the second relocation stage we
122 further reduced absolute location error by combining location information across events based
123 on waveform coherency between the events. This absolute coherency relocation is based on
124 the concept that if the waveforms at a station for two or more events are very similar (have
125 high coherency) up to a given frequency, then the distance separating these “multiplet” events
126 is small relative to the seismic wavelength at that frequency and the events represent stress
127 release on the same, small fault patch (Geller & Mueller, 1980; Poupinet et al., 1982, 1984).

128 The NLL coherence relocation for a target event is a stack over 3D space of the event’s SSST
129 location PDF and the SSST PDF’s for other events, each weighted by the waveform coherency
130 between the target event and the other event. Unlike differential-time based relative location,

131 absolute coherency relocation requires waveforms from as few as one station, allowing precise
132 relocation for sparse networks, and for foreshocks and early aftershocks of a mainshock
133 sequence or swarm before temporary stations are installed. See the Supplementary material
134 Methods S2 for more details.

135 The final coherence locations are shown in Fig. S2b. The median formal errors (e.g. with
136 velocity model fixed and assuming only Gaussian, aleatoric error) for the NLL, NLL-SSST
137 and final, NLL-SSST-coherence locations in both models are listed in Table S1.

138

139 2.2. Matched-filter

140 We used a matched-filter detection algorithm (Gibbons & Ringdal, 2006; Shelly et al., 2007,
141 Vuan, et al., 2018) to improve the magnitude of completeness of the initial catalog and study
142 possible spatio-temporal patterns of the sequence (Vičić et al., 2019).

143 We used waveform data from the 16 closest broadband and short-period stations available for
144 the PR seismic network from the beginning of 2019 until the end of January 2020. The
145 waveform data were filtered between 2 and 8 Hz, where the peak energy of most events is
146 expected and their signal to noise ratio is highest, and downsampled to 20 Hz to speed up
147 processing.

148 We prepared a template catalogue of all initial catalog events with semi-major axis ≤ 5 km for
149 the detection of additional, similar earthquakes. The templates were cut from 2.5s before to
150 2.5s after manually picked S phase arrival times on all available channels and stations. We
151 visually inspected all the templates and removed those of low quality or those that had problems
152 with missing or bad data.

153 To detect new events, the templates were correlated with the continuous waveform data. The
154 sliding-window cross-correlation function (CCF) for each template was calculated with 1
155 sample step. CCFs were calculated for each station and channel for individual templates and
156 then stacked to form a mean daily CCF trace. For a positive detection we set a threshold of
157 $12 \times$ median absolute deviation of the daily trace. After a successful scan of the data we only
158 selected events with inter-event times larger than 3s in order to not include the same event
159 multiple times due to detections from multiple templates. The candidate for detection inside
160 this time window was that with the highest threshold value. The magnitude of the detected
161 event was calculated as the median value of the maximum amplitude ratios for all channels
162 between the template and detected event with a 10-fold increase in amplitude corresponding to
163 a one-unit increase in magnitude (Peng et al., 2009).

164

165 2.3. Kinematic source inversion

166 The sequence included five moderate $5.6 < M_w < 6.4$ events (Fig. S4, Table S2; hereinafter
167 EV#1-EV#5).

168 For kinematic source inversion we used near-field strong motion displacement time series
169 derived from digital three-component accelerograms of the PRSN network (Fig. S4). The
170 displacement data were rotated to a defined cartesian coordinate system and filtered with an a-
171 causal, fourth-order Butterworth filter in the frequency ranges between 0.03 – 0.4 Hz. The
172 selected frequencies depend on the quality of data and the used 1D velocity model of area.

173 The elliptical sub-fault approximation method (Di Carli et al., 2010; Twardzik et al., 2012;
174 Ruiz & Madariaga, 2013; Momeni et al., 2019; Vičić et al., 2020) is used to retrieve the robust
175 features of the ruptures. This method estimates a rupture in a small number of elliptical patches
176 (usually up to three). Nine parameters are enough to define each slip patch: five to define the

177 ellipse geometry (semi-major/minor axes, distance from centre of ellipse, rotation angle of the
178 semi-major axis from horizontal plane, and rotation angle of the ellipse with reference to the
179 nucleation point) and four for slip, rupture speed, rake, and rise time.

180 The inversion process consists of sampling the trial rupture models by the neighbourhood
181 algorithm (Sambridge, 1999a, b) in widely defined ranges for the parameters. Trial synthetic
182 displacement wavefields at each station were computed with Axitra code (Cotton and Coutant,
183 1997). The synthetic wavefields were compared to observations using the Spudich & Miller
184 (1990) cost function which defines a waveform fit in percent. After sufficient iterations of
185 sampling trial models by the adopted algorithm (usually up to 700), we reached convergence
186 to the final model. More details on the inversion procedure are given in Momeni et al. (2019).

187 We used the hypocenters obtained in section 2.1 as initiation points of ruptures (Table 1).
188 Considering the possible errors in hypocenter location and origin time, we allowed the
189 hypocenters to shift ± 1 km along both strike and dip on the fault plane. First, we searched
190 among the nodal planes of the GCMT reported focal mechanism (see Data and Resources) for
191 the geometry of each rupture that provides a rupture model with best waveform-fit to the
192 observations. Selected rupture geometry for all the events are provided in Table 1.

193

194 After selection of geometry for each event, we ran 10 independent inversions each having
195 slightly different model parameters space. With this we investigate different possible rupture
196 models that can provide the same waveform-fit to the observations. The 10 final rupture models
197 for each event are reported in the Supplementary Material S3. For each of the ten rupture
198 models, M_0 and M_w are obtained and the preferred rupture models are chosen based on
199 closeness of their scalar seismic moments to the GCMT and USGS point source inversion
200 results (Fig. 2).

201 2.4. GPS

202 We used the IGS14 position time-series of the continuous GPS (cGPS) stations of the Puerto
203 Rico Island obtained from the repository of the Nevada Geodetic Laboratory (Blewitt et al,
204 2018). The processed network consists of 15 sites (Fig. 3a, Fig S11). We analysed the position
205 time-series (see Data and Resources) following the procedure described in Barzaghi & Borghi,
206 (2018). By considering the temporal correlation among the data and using the least-square
207 estimation method we determined the linear trends (tectonic velocity), seasonal signals,
208 discontinuities due to the station equipment and reference frame changes or seismic events. In
209 Fig. 3a we report the estimated velocity vectors of the cGPS stations for the horizontal
210 components and displacement vectors predicted by NAP. Vertical velocities are mostly
211 positive and are reported in Figure S11. The strain-rate principal axes shows a NS stretching
212 especially across the Great Southern Puerto Rico Fault Zone (GSPRFZ, Piety *et al.*, 2018) (Fig.
213 3c). All of the cGPS stations are characterized by spatial correlation signals, also known as the
214 common mode error (CME). CME can be reduced using different approaches such as the
215 stacking technique (Wdowinski et al., 1997), Principal Component Analysis (PCA), Karhunen-
216 Loeve expansion (KLE) (Dong et al., 2006) and Independent Component Analysis (ICA) (Liu
217 et al., 2015) that represents a Blind Source Separation (BSS) method. These methods,
218 especially PCA and ICA are also used for transient detection as in (Ji & Herring 2013, Borghi
219 *et al.*, 2016, Gualandi *et al.*, 2016, Vičić et al., 2020). Careful investigation is required to
220 discriminate CME and transients in the cGPS time series.

221 For some cGPS stations, data are available from 2006, while others started to operate as late as
222 2017 (Table S7, Fig S12). We focused our investigation in the period from 10th of September
223 2019 to 27th December 2019 because it represents a continuous time range with small data gaps
224 and was characterized by increasing seismicity rate. To increase the signal-to-noise ratio of the
225 data and fill the small gaps, the residual time-series were temporally filtered testing two

226 independent methods: the least-square collocation method (LCS) (Borghi et al., 2009; Borghi
227 et al., 2016) using the covariance functions obtained by the analysis of the temporal correlation,
228 and the moving average method (MA) with data windows of two weeks. As described in the
229 supplementary material the two filtering methods provided analogous results (e.g. Fig. S15).
230 PCA and BSS methods, like FastICA (Liu et al., 2015) and variational Bayesian Component
231 Analysis (vbICA, Choudrey and Roberts, 2003) were applied on the residual time-series for
232 transient signals research and will be discussed in the following section.

233 3. Results and Discussion

234

235 3.1. Geometry of the activated fault system

236 The kinematic source inversion of the five largest ($5.6 < M_w < 6.4$) earthquakes (Fig. 2, Figs. S5-
237 10) and precisely located fore- and aftershocks show that at least five faults were activated.
238 The two dominant parallel faults with WNW-ESE direction ruptured with strike-slip events
239 (EV#1 and EV#4). Southern fault aligns with geologically mapped Punta Montalva fault (Roig-
240 Silva et al., 2013), while the location of the northern fault is less well resolved but lies in an
241 area between two active strike-slip faults – South Lajas fault (Prentice et al., 2005) and Salinas
242 fault (Piety et al., 2018). Depth distribution of seismicity along Punta Montalva fault during
243 this sequence is shallower than 10km and extends for 30km in WNW-ESE direction. Whether
244 or not the Caja swarm lies on the continuation of Punta Montalva fault is difficult to evaluate.
245 If this is the case, a 20km seismic gap exists between the swarm and the activated segment of
246 the fault that ruptured. Depth distribution of seismicity on the northern strike-slip fault is
247 deeper, compared to the Punta Montalva fault, with events between 12 and 22km. The length
248 is around 12km in the WNW-ESE direction.

249 Bounded between two strike-slip faults, two NE-SW striking normal faults (in agreement with
250 the initial InSAR results (for reference see López et al., 2020)) ruptured with the Mw6.4
251 (EV#2) mainshock and the Mw5.6 aftershock (EV#3) that occurred on a fault located 6km E
252 of the mainshock. They do not align with any previously known normal faults (Granja-Bruna
253 et al., 2015).

254 Finally, EV#5 earthquake ruptured a 22km long, NNE-SSW orthogonal strike-slip fault with a
255 unique geometry (discussed in the Conclusions). Northwards it is bounded by the north strike-

256 slip fault while towards south it crosses Punta Montalva fault. The deepest aftershocks are
257 towards the north while the shallowest ones are towards the south (Fig. 1, 2a).

258

259 EV#1 nucleated at the depth of 4.5 ± 1 km. The rupture evolved mostly toward up-dip and
260 slightly to the W with an average rupture velocity of 1.8km/s ($V_s = 3.1$) for ~ 2.6 s. It released
261 a total scalar seismic moment of $5.7E17$ Nm which is comparable to the GCMT and larger than
262 USGS results ($4.5E17$ Nm and $3.16E17$ Nm, respectively). The rake is well resolved (-21°)
263 showing a left-lateral strike-slip mechanism. A maximum slip of 1.8m is observable at the
264 depths of 3 to 4km, between 0.7s and 1.7s after the nucleation. Details (e.g. wave-fit) are
265 presented in the Supplementary Material (S3) for all the studied earthquakes (EV#1-5).

266 EV#2 nucleated at the depth of 8.6km. The rupture evolved on an NE striking (44°) SE dipping
267 (58°) fault plane with an average speed of 1.55km/s. It reached the surface ~ 8 s after the
268 nucleation (Fig. S7b). The rupture occurred in 10s and released a total scalar seismic moment
269 of $5.6E18$ Nm, close to the GCMT and USGS results ($4.72E+18$ Nm and $5.04E+17$ Nm,
270 respectively). It showed a reasonable waveform fit of 75%. Average rake was -124° revealing
271 a normal faulting mechanism with a right-lateral strike-slip component.

272 EV#3 rupture started at the depth of 6.8km. The slip evolved toward shallow depths and slightly
273 to the NE on a NE striking (45°) SE dipping (52°) fault. The whole rupture occurred in 3.3s
274 and released a total scalar seismic moment of $2.74E17$ Nm. The waveform fit was still
275 reasonable (82%) (Fig. S8c).

276 EV#4 nucleated at a depth of 13km. Its slip evolved mostly down-dip and towards E on an \sim E
277 striking, N dipping fault plane with a rupture velocity 2.5km/s, lasting 2.4s with a scalar seismic
278 moment of $6.3E17$ Nm, larger than the GCMT and USGS results ($5.5E17$ Nm and $3.63E17$ Nm,

279 respectively). This model has an 84% waveform fit. The rake is 11° , showing almost pure left-
280 lateral strike-slip mechanism.

281 On the 11th January, EV#5 nucleated at the depth of 19km. Its rupture evolved up-dip and
282 mostly to the N on a ~N-S striking (195°), West dipping (67°) fault plane with an average speed
283 of ~2.8km/s that lasts for ~3.5s. It released a total scalar seismic moment of $1.4E18Nm$. This
284 model has a waveform fit of 89%. The obtained rake was -153° showing a right-lateral strike-
285 slip mechanism with a rise time of ~1.6s.

286

287 3.2. Temporal and spatial evolution

288 Using well located earthquakes as templates we were able to detect additional events, which
289 gave a better understanding of the sequence development.

290 The activity began as a low magnitude ($M < 3.5$) Caja swarm, 14km south of Ponce, Puerto
291 Rico. Caja swarm started in July 2019 and ended in January 2020. The newly detected
292 earthquakes in this swarm were temporally split into 3 bursts of activity (Fig. S17) with the
293 most and largest earthquakes in the third burst. Due to the small magnitudes of the events we
294 were not able to study the swarm in detail.

295 The main part of the Southwestern Puerto Rico sequence initiated along the Punta Montalva
296 fault (Fig. 4a, b), 30 km west of Caja swarm. Prior to the sequence, detected seismicity along
297 the fault was spread over time and we were unable to detect more events than reported in the
298 original catalog.

299 On the 28th December, 2019 a Mw4.7 foreshock, followed by a Mw5.0 earthquake and its
300 aftershock sequence activated the main part of the Southwestern Puerto Rico sequence. After
301 the Mw5.0 the aftershocks slowly extended both in WNW and ESE direction (Fig. 4a) with the

302 migration velocity towards WNW slightly higher than towards ESE. The WNW side of the
303 Punta Montalva fault was more productive in terms of aftershock than its ESE extent. The ESE
304 migration continued until the 6th of January 2020 when the largest, Mw5.8 earthquake took
305 place in the ESE portion of the Punta Montalva fault. The Mw5.8 earthquake was preceded by
306 a foreshock sequence of its own in a 2 km wide area of elevated seismicity less than 1 km away
307 from its hypocentre (Fig. S22). In the aftermath of the Punta Montalva fault earthquake, the
308 aftershocks were distributed all along the previously activated fault segment.

309 On 7th of January, 2020 the Mw6.4 mainshock of the sequence occurred on a normal fault
310 between the Punta Montalva fault and the northern strike-slip fault (Fig. 4b). It was followed
311 by a Mw5.8 normal faulting earthquake NE of its hypocentre. Following the Mw5.8 event, a
312 Mw5.7 strike-slip earthquake ruptured the northern strike-slip fault. The aftershocks along the
313 normal fault were confined towards the north with the area where the fault intersects with the
314 northern strike-slip fault and towards the south, with an intersection with Punta Montalva fault.
315 The aftershock sequence on the normal fault was less energetic than on the northern strike slip
316 fault but this changed on the 8th January, 2020, when a Mw4.7 earthquake took place on it (Fig.
317 4b)

318 On 11th January, an orthogonal fault (Fig. 4b) was activated with a Mw6.0 left-lateral strike
319 slip earthquake. Towards the N, aftershocks were confined by the northern strike slip fault,
320 while towards the S, aftershocks extended past the Punta Montalva fault.

321

322

323

324

325 3.3. Geodetic transients

326 The PCA method applied on the filtered residuals showed that the most important contribution
327 was described by the first two principal components, representing around 80% of the variance.
328 The northern and vertical components are characterized by a discontinuity between October
329 and November 2019, confirmed by Bayesian inference test (Borghini et al., 2012, 2016) on the
330 21st of October, 2019 (day of the year 294 ± 2) with a total probability of 99% (Fig. 3d). A
331 posterior probability related to the Bayesian estimation of the discontinuity is presented in
332 Figure 3d and S15 where we observe the effect of the filtering method used for the detection
333 of discontinuity epoch. PCA and vbICA show very similar behavior in the first principal (PC1)
334 and independent components (IC1) and confirm the individuation of a discontinuity in the
335 northern and vertical components, respectively. The eastern component does not show a sharp
336 discontinuity (Fig. 3d) but rather a positive linear trend that is correlated with the cumulative
337 number of earthquakes in September 2019 (Fig. S17). PC1 could be interpreted as CME signal
338 that should be removed from the time-series, however some considerations suggest that the
339 PCs and ICs reported in Figure 3d and S15 represent a geophysical signal present all over
340 Puerto Rico Island in October 2019. Since all the cGPS contribute to the first components (Fig.
341 S18) we suppose that this corresponds to the complex tectonic signal. Moreover, the observed
342 discontinuity temporally falls in the third burst of Caja swarm, characterized by the most and
343 largest earthquakes (Fig. S17) as already mentioned in Subsection 3.2.

344 Due to the discontinuity corresponding to the period of increasing seismicity, we analysed this
345 period and computed the displacement field related to this event for each station by least square
346 estimation. The displacement field vectors point towards the south (Fig. 3b) while at the same
347 time, stations undergo uplift (Fig. S19). We also note that the principal axes of the 2D strain
348 tensor are not aligned to the principal axes of the strain-rate tensors due to the tectonic velocity
349 of the stations, but rather represent a divergence behaviour in the NE-SW direction (Fig. 3c)

350 **4. Conclusion**

351

352 The geometry defined by the relocated events and inversion of the well recorded Mw5.6+
353 earthquakes on strike-slip and normal faults highlights a very complex system of faulting. We
354 observe that the northern and Punta Montalva faults form a system of parallel strike-slip faults
355 while the normal fault, that hosted the mainshock of the series, forms an oblique structure
356 between them. Additionally, the two parallel strike slip faults are connected by an orthogonal
357 fault deepening from south northward. Its northern edge is bounded by the northern strike-slip
358 fault, while towards the south, it continues past the Punta Montalva fault.

359 These observations show that the geometry of faulting within this sequence is controlled by a
360 larger structural feature – the subduction of CP underneath Puerto Rico (van Benthem et al.,
361 2013) as presented in Figure 5.

362

363 The seismicity on the orthogonal fault follows the subducting CP interface and is most likely
364 constrained by differences between the overriding crust and the CP, such as a transition from
365 velocity weakening in the crust where brittle deformation is promoted to a velocity
366 strengthening regime in the CP that does not allow slip propagation.

367 The discontinuity, observed with PCA analysis and the almost 90° change of displacement
368 vectors in respect to the NAP (Fig. 3a, b) of the cGPS time series, shows that the October 21st
369 2019 transient is common to every station of the island. The long wavelength of observed
370 geodetic transient confirms that the transient originates on a larger scale than localised faulting
371 during the 2019-2020 sequence.

372 The subducting oceanic crust is known to be fluid saturated (Song et al., 2009). If the fluids
373 are released, which happens as a response to the transient perturbations (e.g. slow slip events
374 Audet et al. (2009)), they would migrate from the subducting oceanic crust and drain through
375 permeable fluid conduits (e.g. Fesola et al., 2019) like Punta Montalva or Investigator fault,
376 raising pore pressures and lowering the effective stresses on them, thus generating seismicity
377 (Colella et al., 2017). The resolution of the relocated earthquakes does not allow us to study
378 the Caja swarm in detail, but the low magnitude Caja swarm and the swarm-like behaviour of
379 the main sequence point in the direction of fluids playing an important role. Drainage would in
380 turn control the downdip extent of the seismogenic zone of the subduction. The drier conditions
381 of the subducting interface trenchward would promote fast seismogenic rupture while downdip
382 the strike slip faults, fluid saturation could result in slow slip events within the transition zone
383 (Husker et al., 2018). This could directly influence the seismic hazard of Puerto Rico in case
384 of an earthquake on the Muertos subduction (Byrne et al., 1985).

385 **5. Data and Resources**

386 - The Global Centroid Moment Tensor Project database was searched using
387 www.globalcmt.org/CMTsearch.html (Last accessed March, 2021.)

388 - The repository of the Nevada Geodetic Laboratory was used to obtain the cGPS time
389 series (<http://geodesy.unr.edu>, last accessed June, 2021.)

390 - Dataset of the PR seismic network was accessed through the IRIS DMC archives.
391 (<https://earthquake.usgs.gov>, last accessed May, 2021.)

392

393 The Supplementary to the manuscript includes a detailed descriptions of the methodologies
394 used in the main paper and additional figures for better understanding of both the
395 Supplementary Material and the manuscript. The Supplementary consists of next Sections:

396

397 - **Methods S1. Source-specific station term corrections**

398 - **Methods S2. Absolute, coherency relocation**

399 - **Methods S3. Kinematic rupture inversion**

400 - **Methods S4. GPS**

401 - **Methods S5. Template matching**

402

403 **6. Acknowledgment**

404 B. Vičič and S. Momeni were funded by The Abdus Salam International Centre for
405 Theoretical Physics. A. Lomax's contribution was supported by his personal funds.

406 **7. References**

407

408 Audet, P., Bostock, M. G., Christensen, N. I., & Peacock, S. M. (2009). Seismic evidence for
409 overpressured subducted oceanic crust and megathrust fault sealing. *Nature*, 457(7225), 76-
410 78.

411

412 Barzaghi, R., & Borghi, A. (2018). Theory of second order stationary random processes
413 applied to GPS coordinate time-series. *GPS Solutions*, 22(3), 1–12.

414

415 Benford, B., DeMets, C., & Calais, E. (2012). GPS estimates of microplate motions, northern
416 Caribbean: Evidence for a Hispaniola microplate and implications for earthquake
417 hazard. *Geophysical Journal International*, 191(2), 481-490.

418

419 Benz, H. (2017). Building a National Seismic Monitoring Center: NEIC from 2000 to the
420 present. *Seismological Research Letters*, 88(2A), 265–269.

421

422 Beyreuther, M., Barsch, R., Krischer, L., Megies, T., Behr, Y., & Wassermann, J. (2010).
423 ObsPy: A Python toolbox for seismology. *Seismological Research Letters*, 81(3), 530-533.

424

425 Blewitt, G., Hammond, W. C., & Kreemer, C. (2018). Harnessing the GPS data explosion for
426 interdisciplinary science. *Eos*, 99(10.1029).

427 Borghi, A., Aoudia, A., Riva, R., & Barzaghi, R. (2009). GPS monitoring and earthquake
428 prediction: A success story towards a useful integration. *Tectonophysics*, 465, 177–189,
429 ISSN 0040-1951.

430

431 Borghi, A., Cannizzaro, L., & Vitti, A. (2012). Advanced techniques for discontinuity
432 detection in GNSS coordinate time-series. An Italian case study. In *Geodesy for planet Earth*
433 (pp. 627–634). Berlin, Heidelberg: Springer.

434

435 Borghi, A., Aoudia, A., Javed, F., & Barzaghi, R. (2016). Precursory slow-slip loaded the
436 2009 L'Aquila earthquake sequence. *Geophysical Journal International*, 205, 776–784.

437

438 Byrne, D. B., Suarez, G., & McCann, W. R. (1985). Muertos Trough subduction—Microplate
439 tectonics in the northern Caribbean?. *Nature*, 317(6036), 420-421.

440

441 Chamberlain, C. J., Hopp, C. J., Boese, C. M., Warren-Smith, E., Chambers, D., Chu, S. X.,
442 ... & Townend, J. (2018). EQcorrscan: Repeating and near-repeating earthquake detection
443 and analysis in python. *Seismological Research Letters*, 89(1), 173-181.

444

445 Choudrey, R. A., & Roberts, S. J. (2003). Variational mixture of Bayesian independent
446 component analyzers. *Neural computation*, 15(1), 213-252.

447

448 Colella, H. V., Sit, S. M., Brudzinski, M. R., Graham, S. E., DeMets, C., Holtkamp, S. G., ...
449 & Arciniega-Ceballos, A. (2017). Seismicity rate increases associated with slow slip episodes
450 prior to the 2012 Mw 7.4 Ometepec earthquake. *Earth and Planetary Science Letters*, 464,
451 35-45.

452

453 Cotton, F., & Coutant, O. (1997). Dynamic stress variations due to shear faults in a plane-
454 layered medium. *Geophysical Journal International*, 128(3), 676-688.

455 De Barros, L., Cappa, F., Deschamps, A., & Dublanchet, P. Imbricated Aseismic Slip And
456 Fluid Diffusion Drive A Seismic Swarm In The Corinth Gulf, Greece. *Geophysical Research*
457 *Letters*.

458

459 DeMets, C., Gordon, R. G., & Argus, D. F. (2010). Geologically current plate
460 motions. *Geophysical Journal International*, 181(1), 1-80.

461

462 Di Carli, S., François-Holden, C., Peyrat, S., & Madariaga, R. (2010). Dynamic inversion of
463 the 2000 Tottori earthquake based on elliptical subfault approximations. *Journal of*
464 *Geophysical Research: Solid Earth*, 115(B12).

465

466 Dong, D., Fang, P., Bock, Y., Webb, F., Prawirodirdjo, L., Kedar, S., & Jamason, P. (2006).
467 Spatiotemporal filtering using principal component analysis and Karhunen-Loeve expansion
468 approaches for regional GPS network analysis. *Journal of Geophysical Research*, 111,
469 B03405.

470

471 Doser, D., Rodríguez, C., & Flores, C. (2005). Historical earthquakes of the Puerto Rico-
472 Virgin Island region. Active tectonic and seismic hazards of Puerto Rico, the Virgin Islands,
473 and offshore areas. Mann, P.(Ed.), 103-114.

474

475 Dziewonski, A. M., Chou, T. A., & Woodhouse, J. H. (1981). Determination of earthquake
476 source parameters from waveform data for studies of global and regional seismicity. Journal
477 of Geophysical Research: Solid Earth, 86(B4), 2825-2852.

478

479 Fasola, S. L., Brudzinski, M. R., Holtkamp, S. G., Graham, S. E., & Cabral-Cano, E. (2019).
480 Earthquake swarms and slow slip on a sliver fault in the Mexican subduction zone.
481 Proceedings of the National Academy of Sciences, 116(15), 7198-7206.

482

483 Font, Y., Kao, H., Lallemand, S., Liu, C. S., & Chiao, L. Y. (2004). Hypocentre
484 determination offshore of eastern Taiwan using the Maximum Intersection method.
485 Geophysical Journal International, 158(2), 655-675.

486

487 Geller, R. J., & Mueller, C. S. (1980). Four similar earthquakes in central California.
488 Geophysical Research Letters, 7(10), 821-824.

489

490 Gibbons, S. J., & Ringdal, F. (2006). The detection of low magnitude seismic events using
491 array-based waveform correlation. Geophysical Journal International, 165(1), 149–166.

492

493 Granja-Bruna, J., Muñoz-Martín, A., Ten Brink, U. S., Carbó-Gorosabel, A., Estrada, P. L.,
494 Martín-Dávila, J., ... & Morollón, M. C. (2010). Gravity modeling of the Muertos Trough and
495 tectonic implications (north-eastern Caribbean). *Marine Geophysical Researches*, 31(4), 263-
496 283.

497

498 Granja-Bruna, J., Ten Brink, U. S., Muñoz-Martín, A., Carbó-Gorosabel, A., & Estrada, P. L.
499 (2015). Shallower structure and geomorphology of the southern Puerto Rico offshore
500 margin. *Marine and Petroleum Geology*, 67, 30-56.

501

502 Gualandi, A., Serpelloni, E., & Belardinelli, M. E. (2016). Blind source separation problem in
503 GPS time series. *Journal of Geodesy*, 90(4), 323–341.

504

505 Huérfano, V., & Bataille, K. (1994). Crustal structure and stress regime near Puerto
506 Rico. *Seismic Bulletin: Preliminary locations of earthquakes recorded near Puerto Rico*, 15-
507 19.

508

509 Huérfano, V., von Hillebrandt-Andrade, C., & Báez-Sanchez, G. (2005). Microseismic
510 activity reveals two stress regimes in southwestern Puerto Rico. *Active Tectonics and*
511 *Seismic Hazards of Puerto Rico, the Virgin Islands, and Offshore Areas*, 385, 81-101.

512

513 Huérfano, V. A., Lopez, A. M., Castillo, L., Baez-Sanchez, G., Soto-Cordero, L., Lin, G., &
514 Zhang, Q. (2010). Improving three dimensional velocity model for Puerto Rico-Virgin
515 Islands for rapid earthquake re-locations. AGUFM, 2010, S21B-2031.

516

517 Husker, A., Ferrari, L., Arango-Galván, C., Corbo-Camargo, F., & Arzate-Flores, J. A.
518 (2018). A geologic recipe for transient slip within the seismogenic zone: Insight from the
519 Guerrero seismic gap, Mexico. *Geology*, 46(1), 35-38.

520

521 Jansma, P. E., Mattioli, G. S., Lopez, A., DeMets, C., Dixon, T. H., Mann, P., & Calais, E.
522 (2000). Neotectonics of Puerto Rico and the Virgin Islands, northeastern Caribbean, from
523 GPS geodesy. *Tectonics*, 19(6), 1021-1037.

524

525 Jansma, P.E., Mattioli, G.S., 2005. GPS results from Puerto Rico and the Virgin Islands:
526 constraints on tectonic setting and rates of active faulting. In: Mann, P. (Ed.), *Active*
527 *Tectonics and Seismic Hazards of Puerto Rico, the Virgin Islands, and Offshore Areas.*
528 *Geological Society of America*, pp. 13e30. Special Paper 385.

529

530 Ji, K. H., & Herring, T. A. (2013). A method for detecting transient signals in GPS position
531 time-series: smoothing and principal component analysis. *Geophysical Journal*
532 *International*, 193(1), 171-186.

533

534 Krischer, L., Megies, T., Barsch, R., Beyreuther, M., Lecocq, T., Caudron, C., &
535 Wassermann, J. (2015). ObsPy: A bridge for seismology into the scientific Python
536 ecosystem. *Computational Science & Discovery*, 8(1), 014003.

537

538 Liu, B., Dai, W., Peng, W., & Meng, X. (2015). Spatiotemporal analysis of GPS time series
539 in vertical direction using independent component analysis. *Earth, Planets and Space*, 67(1),
540 1-10.

541

542 Liu, C., Lay, T., Wang, Z., & Xiong, X. (2020). Rupture process of the 7 January 2020, MW
543 6.4 Puerto Rico earthquake. *Geophysical Research Letters*, 47(12), e2020GL087718.

544

545 Lomax, A., Virieux, J., Volant, P., & Berge-Thierry, C. (2000). Probabilistic earthquake
546 location in 3D and layered models. In *Advances in seismic event location* (pp. 101-134).
547 Springer, Dordrecht.

548

549 Lomax, A., Zollo, A., Capuano, P., & Virieux, J. (2001). Precise, absolute earthquake
550 location under Somma–Vesuvius volcano using a new three-dimensional velocity model.
551 *Geophysical Journal International*, 146(2), 313-331.

552

553 Lomax, A. (2005). A reanalysis of the hypocentral location and related observations for the
554 great 1906 California earthquake. *Bulletin of the Seismological Society of America*, 95(3),
555 861-877.

556

557 Lomax, A. (2008). Location of the Focus and Tectonics of the Focal Region of the California
558 Earthquake of 18 April 1906. Location of the Focus and Tectonics of the Focal Region of the
559 Calif. Earthquake of 18 April 1906. *Bulletin of the Seismological Society of America*, 98(2),
560 846-860.

561

562 Lomax, A., Michelini, A., & Curtis, A. (2014). Earthquake Location, Direct, Global-Search
563 Methods. In R. A. Meyers (Ed.), *Encyclopedia of Complexity and Systems Science* (pp. 1–
564 33). New York, NY: Springer New York.

565

566 Lomax, A. (2020). The 2020 Mw 6.5 Monte Cristo Range, Nevada earthquake: relocated
567 seismicity shows rupture of a complete shear-crack system.

568 López A. M., Vanacore E., Hughes K. S., Báez-Sánchez G., and Hudgins T.R. (2020),
569 Response and initial scientific findings from the southwestern Puerto Rico 2020 Seismic
570 Sequence, Temblor

571

572 Momeni, S. M., Aoudia, A., Tatar, M., Twardzik, C., & Madariaga, R. (2019). Kinematics of
573 the 2012 Ahar–Varzaghan complex earthquake doublet (M w6. 5 and M w6. 3). *Geophysical*
574 *Journal International*, 217(3), 2097-2124.

575

576 Peng, Z., & Zhao, P. (2009). Migration of early aftershocks following the 2004 Parkfield
577 earthquake. *Nature Geoscience*, 2(12), 877-881.

578

579 Piety, L. A., Redwine, J. R., Derouin, S. A., Prentice, C. S., Kelson, K. I., Klinger, R. E., &
580 Mahan, S. (2018). Holocene Surface Ruptures on the Salinas Fault and Southeastern Great
581 Southern Puerto Rico Fault Zone, South Coastal Plain of Puerto Rico. Holocene Surface
582 Ruptures on the Salinas Fault and Southeastern GSPRFZ, South Coastal Plain of Puerto
583 Rico. *Bulletin of the Seismological Society of America*, 108(2), 619-638.

584

585 Podvin, P., & Lecomte, I. (1991). Finite difference computation of traveltimes in very
586 contrasted velocity models: a massively parallel approach and its associated tools.
587 *Geophysical Journal International*, 105(1), 271-284.

588

589 Poupinet, G., Glangeaud, F., & Cote, P. (1982, May). P-time delay measurement of a doublet
590 of microearthquakes. In ICASSP'82. *IEEE International Conference on Acoustics, Speech,*
591 *and Signal Processing (Vol. 7, pp. 1516-1519). IEEE.*

592

593 Poupinet, G., Ellsworth, W. L., & Frechet, J. (1984). Monitoring velocity variations in the
594 crust using earthquake doublets: An application to the Calaveras Fault, California. *Journal of*
595 *Geophysical Research: Solid Earth*, 89(B7), 5719-5731.

596

597 Prentice, C. S., & Mann, P. (2005). Paleoseismic study of the South Lajas fault: First
598 documentation of an onshore Holocene fault in Puerto Rico. *Active tectonics and seismic*
599 *hazards of Puerto Rico, the Virgin Islands, and offshore areas: Geological Society of America*
600 *Special Paper*, 385, 215-222.

601

602 Reid, H. F., & Taber, S. (1919). The Porto Rico Earthquake of 1918 with Descriptions of
603 Earlier Earthquakes: Report of the Earthquake Investigation Commission. US Government
604 Printing Office.

605

606 Richards-Dinger, K. B., & Shearer, P. M. (2000). Earthquake locations in southern California
607 obtained using source-specific station terms. *Journal of Geophysical Research: Solid Earth*,
608 105(B5), 10939-10960.

609

610 Spudich, P., & Miller, D. P. (1990). Seismic site effects and the spatial interpolation of
611 earthquake seismograms: results using aftershocks of the 1986 North Palm Springs,
612 California, earthquake. *Bulletin of the Seismological Society of America*, 80(6A), 1504-1532.

613

614 Ruiz, S., & Madariaga, R. (2011). Determination of the friction law parameters of the Mw
615 6.7 Michilla earthquake in northern Chile by dynamic inversion. *Geophysical Research*
616 *Letters*, 38(9).

617

618 Ruiz, S., & Madariaga, R. (2013). Kinematic and dynamic inversion of the 2008 Northern
619 Iwate earthquake. *Bulletin of the Seismological Society of America*, 103(2A), 694-708.

620

621 Sambridge, M. (1999). Geophysical inversion with a neighbourhood algorithm—I. Searching
622 a parameter space. *Geophysical journal international*, 138(2), 479-494.

623

624 Sambridge, M. (1999). Geophysical inversion with a neighbourhood algorithm—II.
625 Appraising the ensemble. *Geophysical Journal International*, 138(3), 727-746.
626

627 Roig-Silva, C. M., Asencio, E., & Joyce, J. (2013). The Northwest Trending North Boquerón
628 Bay-Punta Montalva Fault Zone; A Through Going Active Fault System in Southwestern
629 Puerto Rico. *Seismological Research Letters*, 84(3), 538-550.
630

631 Shelly, D. R., Beroza, G. C., & Ide, S. (2007). Non-volcanic tremor and low-frequency
632 earthquake swarms. *Nature*, 446(7133), 305–307. <https://doi.org/10.1038/nature05666>
633

634 Twardzik, C., Madariaga, R., Das, S., & Custódio, S. (2012). Robust features of the source
635 process for the 2004 Parkfield, California, earthquake from strong-motion
636 seismograms. *Geophysical Journal International*, 191(3), 1245-1254.
637

638 Song, T. R. A., Helmberger, D. V., Brudzinski, M. R., Clayton, R. W., Davis, P., Pérez-
639 Campos, X., & Singh, S. K. (2009). Subducting slab ultra-slow velocity layer coincident with
640 silent earthquakes in southern Mexico. *Science*, 324(5926), 502-506.
641

642 University of Puerto Rico (1986): Puerto Rico Seismic Network & Puerto Rico Strong
643 Motion Program. International Federation of Digital Seismograph Networks. Dataset/Seismic
644 Network. 10.7914/SN/PR
645

646 van Benthem, S., Govers, R., Spakman, W., & Wortel, R. (2013). Tectonic evolution and
647 mantle structure of the Caribbean. *Journal of Geophysical Research: Solid Earth*, 118(6),
648 3019-3036.

649

650 Vičič, B., Aoudia, A., Javed, F., Foroutan, M., & Costa, G. (2019). Geometry and mechanics
651 of the active fault system in western Slovenia. *Geophysical Journal International*, 217(3),
652 1755-1766.

653

654 Vičič, B., Aoudia, A., Borghi, A., Momeni, S., & Vuan, A. (2020). Seismicity rate changes
655 and geodetic transients in Central Apennines. *Geophysical Research Letters*, 47(22),
656 e2020GL090668.

657 Vuan, A., Sukan, M., Amati, G., & Kato, A. (2018). Improving the Detection of Low-
658 Magnitude Seismicity Preceding the Mw 6.3 L'Aquila Earthquake: Development of a
659 Scalable Code Based on the Cross Correlation of Template. *Bulletin of the Seismological*
660 *Society of America*, 108(1), 471-480.

661

662 Waldhauser, Felix, and William L. Ellsworth. "A double-difference earthquake location
663 algorithm: Method and application to the northern Hayward fault, California." *Bulletin of the*
664 *Seismological Society of America* 90.6 (2000): 1353-1368.

665

666 Wdowinski, S., Bock, Y., Zhang, J., Fang, P., & Genrich, J. (1997). Southern California
667 permanent GPS geodetic array: Spatial filtering of daily positions for estimating coseismic

668 and postseismic displacements induced by the 1992 Landers earthquake. *Journal of*
669 *Geophysical Research*, 102(B8), 18,057–18,070.

670

671 Xu, X., Keller, G. R., & Guo, X. (2016). Dip variations of the North American and North
672 Caribbean Plates dominate the tectonic activity of Puerto Rico–Virgin Islands and adjacent
673 areas. *Geological Journal*, 51(6), 901-914.

674

675 Zhou, H. W. (1994). Rapid three-dimensional hypocentral determination using a master
676 station method. *Journal of Geophysical Research: Solid Earth*, 99(B8), 15439-15455.

677

678 **Full postal address for authors:**

679 **Blaž Vičič:**

680 The Abdus Salam International Centre for Theoretical Physics, Strada Costiera 11, I-34151

681 Trieste, Italy

682 **Seyyedmaalek Momeni:**

683 The Abdus Salam International Centre for Theoretical Physics, Strada Costiera 11, I-34151

684 Trieste, Italy

685 Ecole Polytechnique Fédérale de Lausanne, Geo-Energy Laboratory, Route Cantonale, 1015

686 Lausanne, Switzerland

687 **Alessandra Borghi:**

688 The Abdus Salam International Centre for Theoretical Physics, Strada Costiera 11, I-34151

689 Trieste, Italy

690 Istituto Nazionale Geofisica e Vulcanologia, sezione di Bologna, Via Franceschini 31, 40128

691 Bologna, Italy

692 **Anthony Lomax**

693 ALomax Scientific, 320 Chemin des Indes, 06370 Mouans-Sartoux, France

694 **Abdelkrim Aoudia:**

695 The Abdus Salam International Centre for Theoretical Physics, Strada Costiera 11, I-34151

696 Trieste, Italy

697

698 8. Figure Legend

699 **Figure 1:** The 2019-2020 Southwest Puerto Rico earthquake sequence colored by depth .The red lines represent
700 known faults. Offshore faults are from Granja-Bruna et al. (2015).The inset figure shows generalized tectonic regime.
701 Figures A and B correspond to the NNE-SSW and ESE-WNW profiles respectfully.

702 **Figure 2:** Extended rupture models as obtained for the mainshock (EV#2) and b) fore- (EV#1) and aftershocks
703 (EV#3-5) and c) their superimposition. Colored circles are the seismicity shown in Figure 1. Colors of small
704 earthquakes and moment tensors represent their depths and centroid depths, respectfully. Stars are the hypocenters of
705 the five largest events (this study). Focal mechanisms of the respective events are listed in Table 1. Red dashed line is
706 the surface projection of the mainshock fault. Red nodal planes are the fault planes geometry (this study). Thin black
707 line is the shoreline.

708 **Figure 3:** Absolute horizontal velocities (black arrows) and displacement vectors predicted by NAP (blue arrows).
709 b) Estimate of the horizontal deformation in the time window analyzed for the duration of the transient signal pointed
710 out by the BSS at time 21st October 2019 in respect to the NAP. c) The blue arrows represent the planar strain-rate
711 values obtained by the estimated velocity, whereas the red arrows are the principal axis of the strain tensor due to the
712 transient recorded on 21st October, 2019. The red lines are the faults. d) The first Principal component (PC1, red line)
713 and the first Independent Component (vbIC1, blue dots) for the three coordinate components (North, East, Up). The
714 vertical lines (October 21st 2019) represents the discontinuities pointed out in the North component by a Bayesian
715 inference test.

716 **Figure 4:** Top figure shows evolution of seismicity, detected by matched filtering, along the strike of strike-slip
717 faults, highlighting the features of Punta Montalva fault and northern strike slip fault. Bottom figure shows seismicity,
718 detected by matched filtering, along the strike of orthogonal strike-slip fault, highlighting the evolution of seismicity on
719 the normal fault that ruptured with the Mw6.4 mainshock and along the orthogonal strike slip fault.

720 **Figure 5:** A SSW-NNE profile (profile A, Fig. 1) over the SW part of the Puerto Rico Island. The full red line
721 represents the subduction interface (Granja-Bruna et. al, 2015), while the dotted red line represents inferred subduction
722 dipping towards the north.

723

724 **Table 1.** Rupture inversion information and results for the five largest earthquakes of the 2020 Puerto-Rico
 725 seismic sequence.

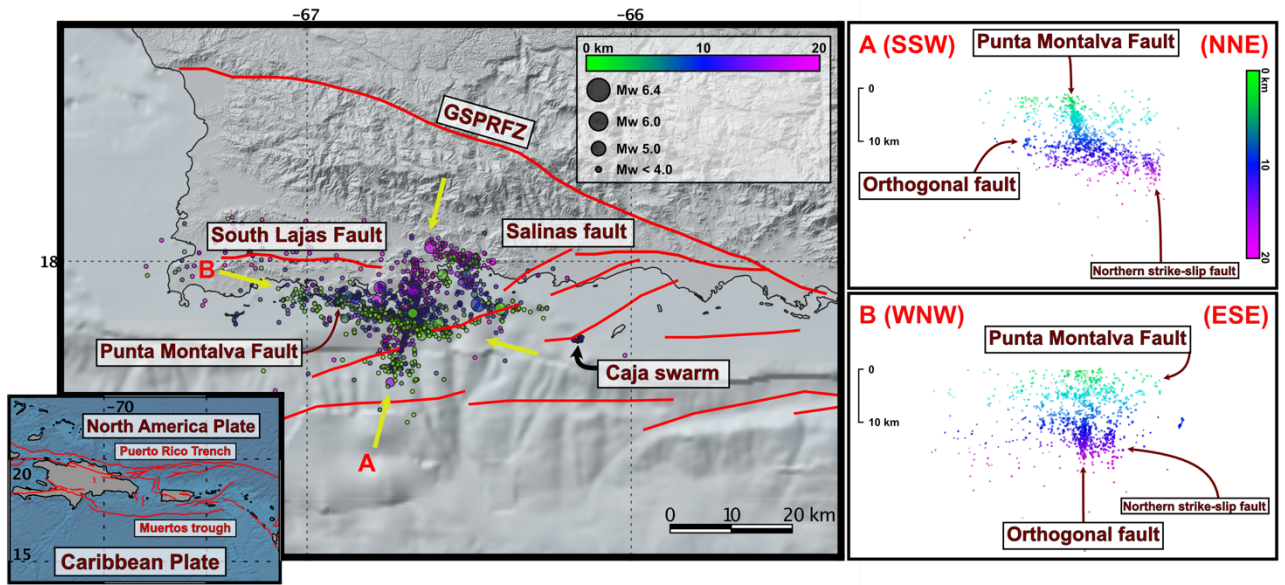
Event #	Date yyyy/mm/d	Time hh:mm:ss	Lat. (°)	Long. (°)	Mag. (Mw)	Depth (km)	Strike (°)	Dip (°)	Rake (°)	Freq (min-max) Hz	M0 (Nm)
1	2020/01/06	10:32:23	17.899	-66.809	5.7	4.5	284	59	-20	0.05-0.2	5.7 E+17
2	2020/01/07	08:24:31	17.931	-66.790	6.4	8.6	44	58	-122	0.03-0.4	5.6 E+18
3	2020/01/07	08:34:05.8	17.934	-66.736	5.6	6.84	45	52	-118	0.06-0.2	2.7 E+17
4	2020/01/07	11:18:46.7	18.009	-66.768	5.8	13.25	296	69	11	0.05-0.3	6.3 E+17
5	2020/01/11	12:54:49.5	17.894	-66.849	6.0	18.72	195	67	-153	0.05-0.3	1.4 E+18

726

727

728

729



730

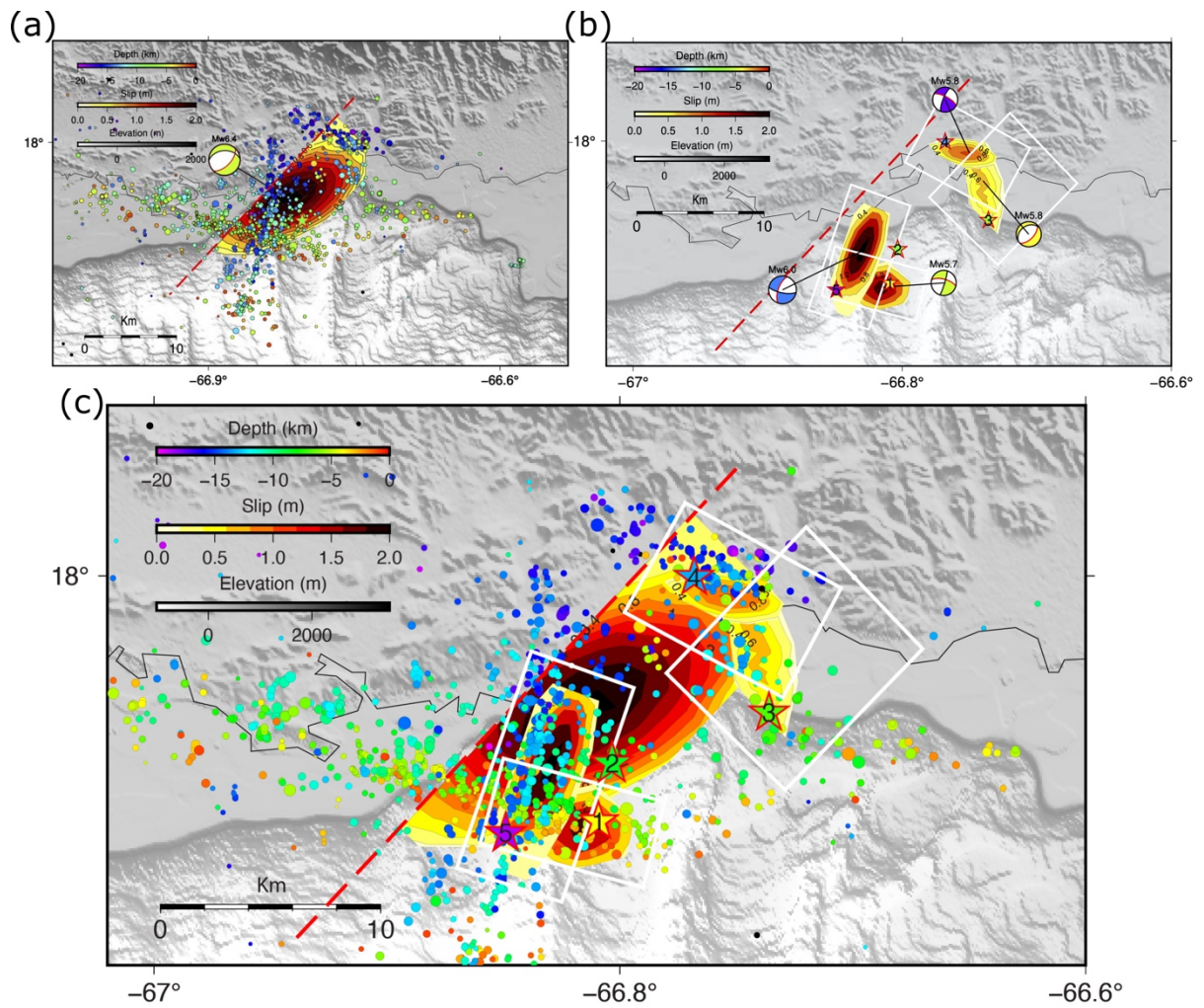
731

732

733

734

Figure 1: The 2019-2020 Southwest Puerto Rico earthquake sequence colored by depth .The red lines represent known faults. Offshore faults are from Granja-Bruna et al. (2015).The inset figure shows generalized tectonic regime. Figures A and B correspond to the NNE-SSW and ESE-WNW profiles respectively.



735

736

737

738

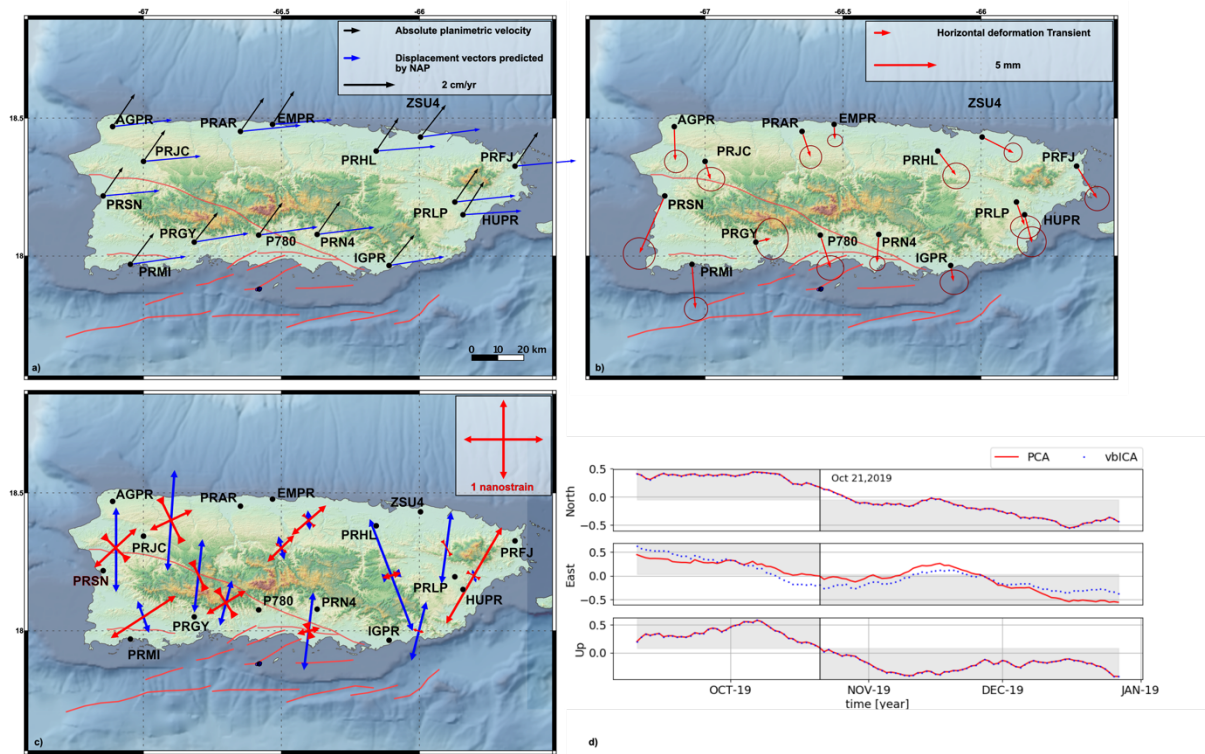
739

740

741

742

Figure 2: Extended rupture models as obtained for the mainshock (EV#2) and b) fore- (EV#1) and aftershocks (EV#3-5) and c) their superimposition. Colored circles are the seismicity shown in Figure 1. Colors of small earthquakes and moment tensors represent their depths and centroid depths, respectively. Stars are the hypocenters of the five largest events (this study). Focal mechanisms of the respective events are listed in Table 1. Red dashed line is the surface projection of the mainshock fault. Red nodal planes are the fault planes geometry (this study). Thin black line is the shoreline.



743

744 **Figure 3:** Absolute horizontal velocities (black arrows) and displacement vectors predicted by NAP (blue arrows). b)

745 Estimate of the horizontal deformation in the time window analyzed for the duration of the transient signal pointed out by the

746 BSS at time 21st October 2019 in respect to the NAP. c) The blue arrows represent the planar strain-rate values obtained by

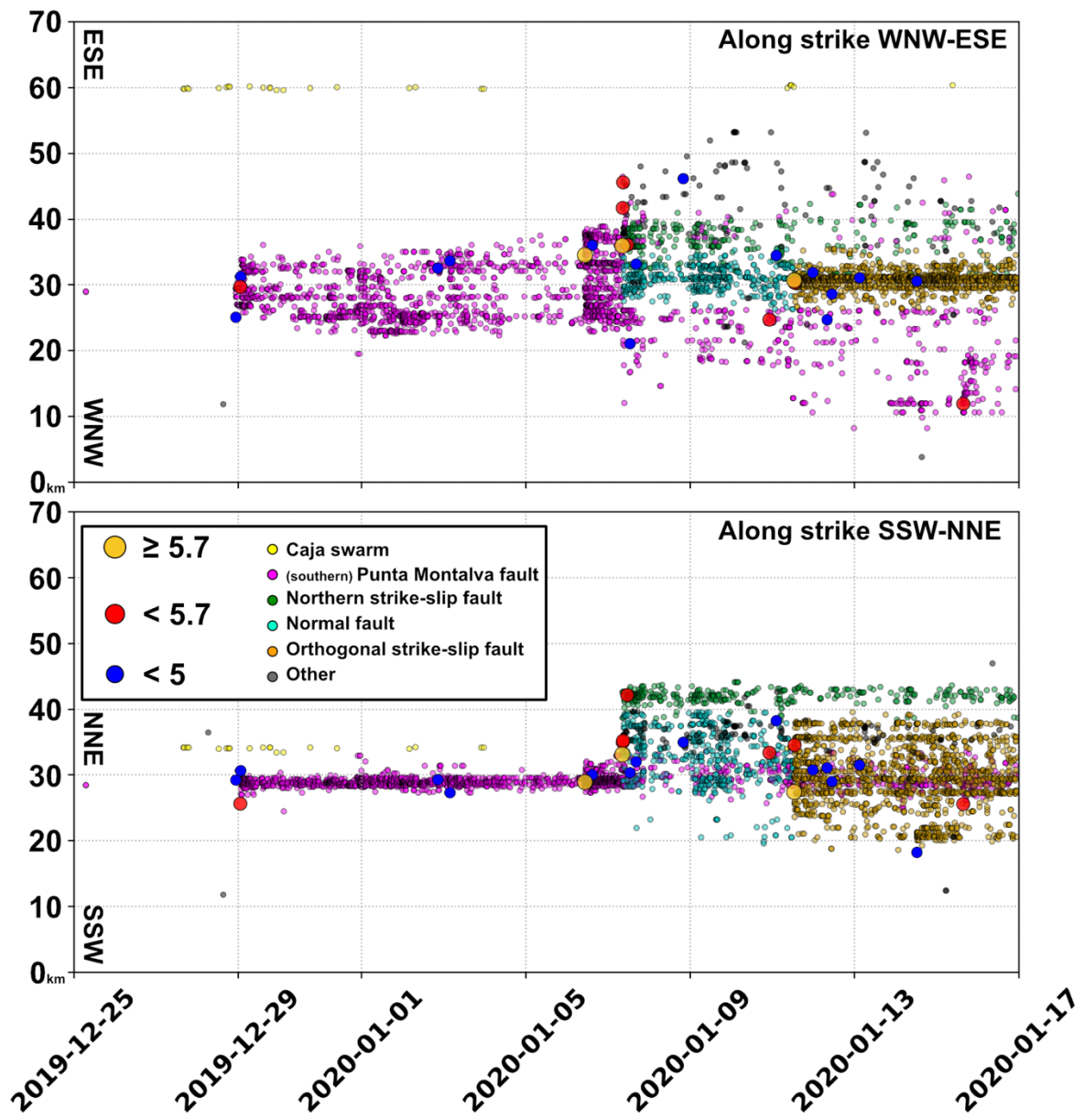
747 the estimated velocity, whereas the red arrows are the principal axis of the strain tensor due to the transient recorded on 21st

748 October, 2019. The red lines are the faults. d) The first Principal component (PC1, red line) and the first Independent

749 Component (vbIC1, blue dots) for the three coordinate components (North, East, Up). The vertical lines (October 21st 2019)

750 represents the discontinuities pointed out in the North component by a Bayesian inference test.

751



752

753

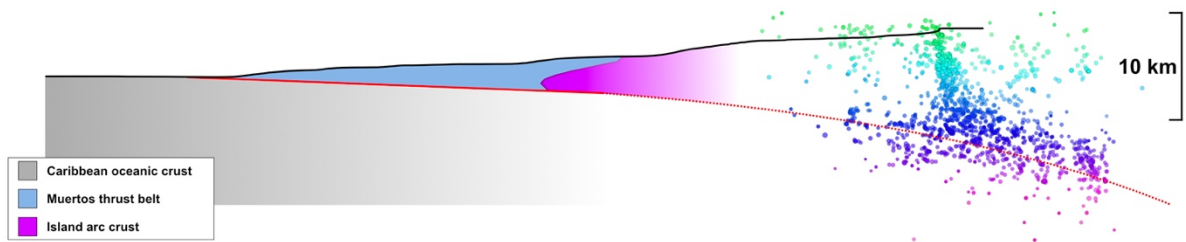
754

755

756

Figure 4: Top figure shows evolution of seismicity, detected by matched filtering, along the strike of strike-slip faults, highlighting the features of Punta Montalva fault and northern strike slip fault. Bottom figure shows seismicity, detected by matched filtering, along the strike of orthogonal strike-slip fault, highlighting the evolution of seismicity on the normal fault that ruptured with the Mw6.4 mainshock and along the orthogonal strike slip fault.

757



758

Figure 5: A SSW-NNE profile (profile A, Fig. 1) over the SW part of the Puerto Rico Island. The full red line

759

represents the subduction interface (Granja-Bruna et. al, 2015), while the dotted red line represents inferred subduction

760

dipping towards the north.